Extreme Mechanics Letters 56 (2022) 101849

Contents lists available at ScienceDirect

Extreme Mechanics Letters

journal homepage: www.elsevier.com/locate/eml

Deployment and surface accuracy of regularly creased membranes

M. Gori [a], F. Bosi [b,*]

[a] NASA Jet Propulsion Laboratory, California Institute of Technology, Pasadena, CA 91109, United States of America
[b] Department of Mechanical Engineering, University College London, London, WC1E 6BT, United Kingdom

ARTICLE INFO

Article history:
Received 31 May 2022
Received in revised form 11 July 2022
Accepted 19 July 2022
Available online 27 July 2022

Keywords:
Origami
Crease
Thin films
Membrane structures
Elastica
Folding

ABSTRACT

Creases are highly localized regions ubiquitous across different length scales in low-dimensional natural and engineering systems. Their presence strongly influences the mechanical response and surface accuracy of creased membrane materials and structures. In this paper, we study the deployment of folded sheets composed of an arbitrary number of non-interacting and parallel creases. We develop a mathematical formulation that describes the nonlinear mechanics of systematically creased membranes composed of a single or multiple folds, and predicts their surface accuracy during unfolding. The proposed solution shows the contribution of membrane bending and crease energies during deployment, and reveals the presence of two dimensionless parameters that govern the unfolding behaviour. Sensitivity analyses are also performed to assess the influence of the crease geometry and constitutive behaviour. The analytical predictions are validated through finite element analyses and deployment tests performed on thin films with one, two and three fold lines, where imaging techniques are employed to quantify deformation. The excellent agreement between theoretical and experimental results testifies that the developed formulation represents a precise tool to assess the tensioning of creased membranes, with applications ranging from origami metamaterials to lightweight space structures where precise shape control is paramount.

© 2022 The Author(s). Published by Elsevier Ltd. This is an open access article under the CC BY license (http://creativecommons.org/licenses/by/4.0/).

1. Introduction

Folds and creases are localized inelastic regions found in thin systems across nature and man-made structures. In biology and living matters, they span different length scales and can be found in the structure of proteins [1], insect wings [2], plant leaves [3] and human skin [4]. In artificial systems, folds are introduced to create mechanical metamaterials [5–7], pieces of art [8] and engineering structures [9–11] through origami techniques. In particular, the Japanese art of paper folding has inspired efficient packaging of lightweight membrane space structures [12,13], such as solar sails, reflectors, and space antennas, which are then deployed once in orbit. However, the introduction of inelastic creases deeply affects the shape configuration and stability of deployed membrane structures and creased metamaterials, hindering their surface accuracy and structural behaviour [14–16]. Therefore, correct modelling of creased thin films is necessary to understand how creases affect the mechanical and functional responses, to suggest optimal folding techniques, and to design the next generation of creased engineering systems.

Systematically creased systems were initially kinematically modelled by rigid panels connected through hinges [17,18], thus neglecting the panel deformation inherently present in folded thin-film structures. Hence, linear analytical [19] and nonlinear numerical [20] models based on beam theory were introduced to capture the elastic response of the membrane. However, these models neglect the crease compliance, as the fold was characterized only by its initial opening angle. The importance of modelling both the crease and panel elastic responses showed the contribution of each mechanism during deployment, and highlighted the existence of a characteristic length scale below which the membrane deformation can be neglected, and the mechanical response can be approximated by a rigid-folded mechanism [21]. Experimental studies on different materials have shown a linear moment–angle relationship at the crease, which can be modelled as a rotational spring with constant stiffness [21–23]. Its constitutive behaviour and elastic contribution were included in a nonlinear beam framework aimed at obtaining the mechanical response of membranes with a single crease [23–25]. Recent works have improved the fold characterization by analysing the formation [22] and local response [26] of folds, their inelastic behaviour [27] and the viscoelastic effects on the initial opening angle [28]. They have proven that the highly localized plasticity at the fold and the material viscosity mainly affect the crease stiffness and initial crease opening, with negligible influence on the elasticity and deployment of the membrane.

The recent advances on the monodimensional modelling of creased membranes considered sheets with a single fold and did

* Corresponding author.
E-mail addresses: marcello.gori@jpl.nasa.gov (M. Gori), f.bosi@ucl.ac.uk (F. Bosi).

https://doi.org/10.1016/j.eml.2022.101849
2352-4316/© 2022 The Author(s). Published by Elsevier Ltd. This is an open access article under the CC BY license (http://creativecommons.org/licenses/by/4.0/).

not compute the surface accuracy during deployment, which is required to design the tensioning mechanisms of large creased membrane-based space systems that can attain precise submillimetre shape control. Therefore, this paper establishes a nonlinear plane strain solution for the deployment of accordion-like shaped membranes characterized by an arbitrary number of noninteracting and alternating mountain–valley folds, which represents the simplest origami configuration. The one-dimensional finite rotation crease-beam mathematical model, which is also capable of predicting the thin film surface accuracy during unfolding, is numerically and experimentally validated through tension tests performed with 2D and 3D digital image correlation. Furthermore, previous studies [21,23] characterized the contributions of panel bending and crease opening through a linear analysis and showed that a single parameter could describe the primary unfolding mechanism. In this work, by considering the energy contributions obtained from a fully nonlinear analysis, we show that two dimensionless parameters are required to capture the interaction between membrane and crease elasticities during deployment, offering tools to evaluate them.

The paper is organized as follows: Section 2 presents the nonlinear mathematical formulation to model the deployment of membranes with a single and multiple creases, including their surface accuracy and contribution of bending and crease energies. Section 3 offers an overview of the numerical and experimental procedures employed; while Section 4 reports the results on the (i) fold rotational stiffness and the influence of initial opening angle and crease rigidity, (ii) comparison between theoretical predictions and experimental measurements during the deployment of membranes with one, two and three creases, and (iii) the effect of energy contributions on the unfolding mechanism.

2. Nonlinear mechanics of creased sheets

We consider homogeneous elastic rectangular membranes with width w and thickness t, longitudinally folded in order to create parallel and alternating mountain ($\wedge$-shape) and valley ($\vee$-shape) creases in the transverse direction, Fig. 1. The creased thin sheet is pinned at one edge and simply supported at the other edge, where a tensile force F acts in the X-direction. The length of the membrane between two consecutive creases is $2l$. In the undeformed configuration, each side of the fold is flat, so that the membrane assumes an accordion-like shape characterized by the crease initial opening angle γ_0, or equivalently by the angle $\alpha = (\pi-\gamma_0)/2$ that the flat panels form with the X-axis. The formation of the creases is caused by highly-localized deformations, and the fold line is assumed to behave as a linear elastic hinge during deployment [21–23], as experimentally proven in Section 4.1 and Appendix B. Therefore, the constitutive relation of the fold writes as $M_c = k\,(\gamma - \gamma_0)$, where M_c is the absolute value of bending moment at the crease, k and γ are the crease rotational stiffness and opening angle, respectively. The symmetry of the membrane with respect to the fold line implies that the rotations at each side of the crease, θ_c^- and θ_c^+, are equal in modulus and opposite in sign, so that $\gamma = \gamma_0 + 2\theta_c$ and $M_c = 2\,k\,\theta_c$.

The mechanical response of creased membranes depends on the interplay between the fold rotational stiffness k and the panels bending rigidity B [21], as further explained in Section 2.4. If the former contribution is dominant, the membrane response is kinematically described by an origami-like rigid mechanism [17]; whereas, when the latter prevails, the deformation is driven by the sheet elasticity, similar to a tensioned thin film or a fluid meniscus in a capillary channel [29]. In this work, both elastic contributions affect the behaviour of the creased membranes, which can be studied as a two-dimensional profile due to the translational symmetry. Therefore, in the following, Euler's theory of the Elastica will be employed to describe the mechanics of the creased sheet as an elastic inextensible rod [30,31] and to develop a plane strain crease-beam model.

2.1. Single crease model

With reference to the two-dimensional single crease system reported in Fig. 1c, the membrane is parametrized by the curvilinear coordinate $s \in [0, 2l]$ and the local angles $\theta_1(s)$ and $\theta_2(s)$ between the tangent vector to the membrane and the local axes x_1 and x_2 on the left- and right-end side of the fold, respectively. The undeformed configuration assumes a $\wedge$-shape, where α represents the angle between the flat panels and the global horizontal axis X. The system is pinned at the left end and simply supported at the right end, where an horizontal tensile force F is applied in the positive X direction. The crease is modelled as a rotational spring of stiffness k at $s = l$ and, due to symmetry, the vertical reaction forces at the supports are null. Thus, under the inextensibility constraints $x_i'(s) = \cos\theta_i(s)$ and $y_i'(s) = \sin\theta_i(s)$ for $i = 1, 2$, the potential energy $\mathcal{V}$ can be written as [32,33]

$$\begin{aligned}\mathcal{V}(\theta_1,\theta_2) =& \frac{B}{2}\left[\int_0^l \theta_1'^2 \mathrm{d}s + \int_l^{2l} \theta_2'^2 \mathrm{d}s\right] + \frac{k}{2}\left[\theta_2(l) - \theta_1(l)\right]^2 \\ &+ F\cos\alpha\left[2l - \int_0^l \cos\theta_1 \mathrm{d}s - \int_l^{2l}\cos\theta_2 \mathrm{d}s\right] \\ &+ F\sin\alpha\left[\int_0^l \sin\theta_1 \mathrm{d}s - \int_l^{2l}\sin\theta_2 \mathrm{d}s\right],\end{aligned} \tag{1}$$

where $\theta' = \mathrm{d}\theta/\mathrm{d}s$ represent the curvature, $B = E\,w\,t^3/[12(1-\nu^2)]$ is the bending stiffness, E the Young's modulus and ν is the Poisson's ratio. In the previous expression, the terms in the first two brackets represent the elastic energy of the membrane and the crease, respectively, while the last terms refer to the work done by the external load F. The equilibrium equations for the first and second half of the membrane, identified by $i = 1$ and $s = [0, l]$, and $i = 2$ and $s = [l, 2l]$, can be obtained by annealing the first variation of $\mathcal{V}$ as

$$B\theta_i'' + (-1)^i F \sin\left[(-1)^i\theta_i + \beta\right] = 0, \tag{2}$$

where $\beta = \pi - \alpha$ represents a supplementary angle. The former nonlinear differential equations can be solved by considering the boundary condition at the crease $(-1)^i B\theta_i'(l) = 2k\theta_i(l)$, and those at the edges, $\theta_1'(0) = 0$ and $\theta_2'(2l) = 0$. Following the derivation outlined in Appendix A, and introducing the dimensionless curvilinear coordinate $\hat{s} = s/l$ and load $\lambda^2 = Fl^2/B$, the membrane's local rotational field results

$$\theta_i(\hat{s}) = (-1)^i\left(2\arcsin\left[\eta\,\mathrm{sn}\left(\lambda(\hat{s} - 2\mathcal{H}(i-1)) + \mathcal{K}(\eta), \eta\right)\right] - \beta\right), \tag{3}$$

where $\mathcal{H}(i-1)$ is the Heaviside step function, sn represents the Jacobi sine amplitude function, and $\mathcal{K}(\eta)$ is the complete elliptic integral of the first kind. The kinematic parameter $\eta = \sin[(\theta(0)+\beta)/2]$ can be obtained as a function of the load λ by solving numerically the following auxiliary equation, obtained from the boundary condition at the crease [34]

$$-2\arcsin\left[\eta\,\mathrm{sn}\left(\lambda + \mathcal{K}(\eta), \eta\right)\right] + \beta - \frac{\lambda\,\eta\,\mathrm{cn}\left(\lambda + \mathcal{K}(\eta), \eta\right)}{\chi} = 0, \tag{4}$$

where $\chi = kl/B$ is the dimensionless rotational stiffness and cn represents the Jacobi cosine amplitude function. In the global reference frame, the membrane's rotation field is $\psi(\hat{s}) = \theta_i(\hat{s}) - (-1)^i\alpha$, whereas the configuration of the deformed elastica is described by the dimensionless coordinates $\hat{X}$ and $\hat{Y}$ for $\hat{s} \in [0, 2]$

$$\begin{aligned}\hat{X}(\hat{s}) =& \hat{s} + \frac{2}{\lambda}\left[\mathcal{E}(\eta) - \mathcal{E}\left(\mathrm{am}(\lambda(\hat{s} - 2\mathcal{H}(i-1)) + \mathcal{K}(\eta), \eta), \eta\right)\right. \\ &\left. + 2\mathcal{H}(i-1)\left(\mathcal{E}\left(\mathrm{am}(\mathcal{K}(m,\eta),\eta),\eta\right) - \mathcal{E}(\eta)\right)\right], \\ \hat{Y}(\hat{s}) =& (-1)^i\,\mathrm{cn}\left(\lambda(\hat{s} - 2\mathcal{H}(i-1)) + \mathcal{K}(\eta), \eta\right),\end{aligned} \tag{5}$$

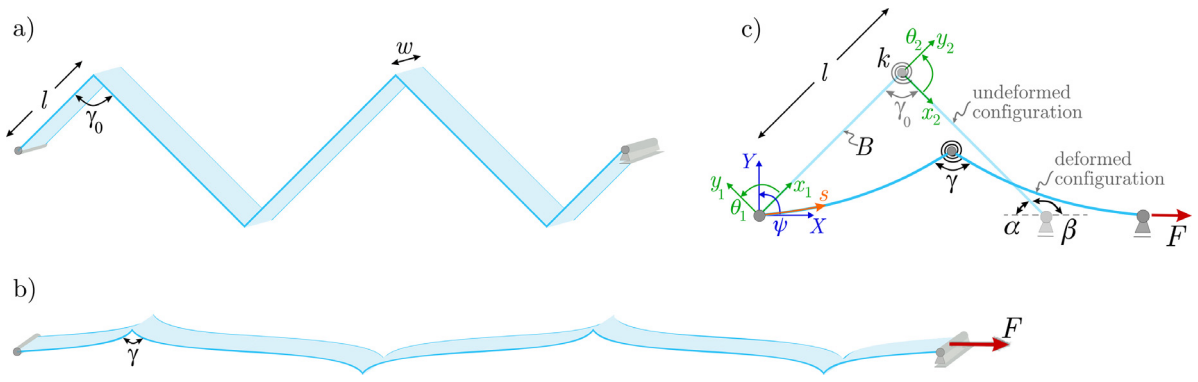

Fig. 1. Undeformed (a) and deformed (b) configurations of a membrane with multiple mountain and valley creases, subjected to a tensile force F. (c) Schematic of the undeformed and deformed shapes of symmetric two-dimensional single crease system, reproducing the behaviour of the membrane with multiple folds. The beam's nonlinear response is driven by the elasticity of the sheet, B, and that of the crease, modelled as an elastic rotational spring of stiffness k and initial opening angle γ_0.

where $\mathcal{K}(m,\eta)$ is the incomplete elliptic integrals of the first kind, $\mathcal{E}(\eta)$ and $\mathcal{E}(m,\eta)$ are the complete and incomplete elliptic integrals of the second kind, am represents the Jacobi amplitude function, and $m = \sin^{-1}[\sin[(\theta_2(0)+\beta)/2]/\eta]$. Lastly, the dimensionless horizontal, $\hat{u}_c$, and vertical, $\hat{v}_c$, displacements of the crease ($\hat{s}=1$) can be obtained in the global reference frame as

$$\begin{aligned}\hat{u}_c &= \frac{1}{\lambda}\left[2\mathcal{E}(m,\eta) - 2\mathcal{E}(\eta) + (\cos\alpha - 1)\left(\mathcal{K}(m,\eta) - \mathcal{K}(\eta)\right)\right],\\ \hat{v}_c &= \frac{2\eta}{\lambda}\cos m - \sin\alpha,\end{aligned} \tag{6}$$

from which it follows that the dimensionless horizontal displacement at the loaded end of the membrane is $\hat{\delta} = 2\hat{u}_c$.

2.2. Multiple creases model

The equations describing the equilibrium configuration of the membrane with a single crease are generalized in this section to describe the response of a tensioned sheet with an arbitrary number of folds $\mathcal{F}$, Fig. 1a. Since the length of the thin sheet between two consecutive creases is $2l$, the total length of the membrane is $2\mathcal{F}l$. Denoting $\hat{s} \in [0, 2\mathcal{F}]$ as the dimensionless curvilinear coordinate along the membrane longitudinal axis, the parameter $\mathcal{N} = \mathbb{Z}[(1+\hat{s})/2]$ describes the progressive number of folds encountered, starting from the pinned support. Hence, $\mathcal{N} = 0$ for $\hat{s} \in [0,1]$ (between the pinned support and the first mountain fold, $\hat{s}=1$), $\mathcal{N}=1$ for $\hat{s}\in[1,3]$ (between the first mountain and second valley folds), $\mathcal{N}=2$ for $\hat{s}\in[3,5]$ (between the second valley and third mountain folds), and so on and so forth. The undeformed configuration of the membrane, characterized by flat segments between alternating transverse mountain ($\wedge$-shape) and valley ($\vee$-shape) creases can be described by the dimensionless global coordinates as $\hat{X}_{\text{undef}}(\hat{s}) = \hat{s}\cos\alpha$ and $\hat{Y}_{\text{undef}}(\hat{s}) = (-1)^{\mathcal{N}}\sin\alpha\,(s-2\mathcal{N})$. The membrane's local, $\theta(\hat{s})$, and global, $\psi(\hat{s})$, rotational fields can be written as

$$\begin{aligned}\theta(\hat{s}) &= (-1)^{\mathcal{N}}\left[\beta - 2\arcsin\left[\eta\,\mathrm{sn}\left(\lambda(\hat{s}-2\mathcal{N}) + \mathcal{K}(\eta),\eta\right)\right]\right],\\ \psi(\hat{s}) &= (-1)^{\mathcal{N}}\left[\pi - 2\arcsin\left[\eta\,\mathrm{sn}\left(\lambda(\hat{s}-2\mathcal{N}) + \mathcal{K}(\eta),\eta\right)\right]\right],\end{aligned} \tag{7}$$

while the deformed configuration of the tensioned thin sheet can be obtained by considering the properties of elliptic integrals $\mathcal{E}(\mathrm{am}(2\mathcal{K}\pm\mu)) = 2\mathcal{E}\pm\mathcal{E}(\mathrm{am}(\mu))$ and $\mathrm{cn}(\mu+\mathcal{K},\eta) = -\sqrt{1-\eta^2}\,\mathrm{sd}(\mu,\eta)$ [35]

$$\begin{aligned}\hat{X}(\hat{s}) &= \hat{s} + \frac{2}{\lambda}\left[\mathcal{E}(\eta) - \mathcal{E}\left(\mathrm{am}(\lambda(\hat{s}-2\mathcal{N}) + \mathcal{K}(\eta),\eta),\eta\right)\right.\\ &\quad \left. + 2\mathcal{N}\left(\mathcal{E}\left(\mathrm{am}(\mathcal{K}(\eta)-\lambda,\eta),\eta\right) - \mathcal{E}(\eta)\right)\right],\\ \hat{Y}(\hat{s}) &= (-1)^{\mathcal{N}}\frac{2\eta}{\lambda}\sqrt{1-\eta^2}\,\mathrm{sd}\left(\lambda(\hat{s}-2\mathcal{N}),\eta\right),\end{aligned} \tag{8}$$

where $\mathrm{sd} = \mathrm{sn}/\mathrm{dn}$ is a Jacobi elliptic function defined through the Jacobi delta amplitude, $\mathrm{dn} = \sqrt{1-\eta^2\mathrm{sn}^2}$. Finally, the dimensionless horizontal displacement of the loaded support is $\hat{\delta} = 2\mathcal{F}\hat{u}_c$, with $\hat{u}_c$ expressed by Eq. $(6)_1$, whereas the absolute value of the dimensionless vertical displacement of any crease, $\hat{v}_c$, is described by Eq. $(6)_2$.

2.3. Surface accuracy during deployment

Several high-precision engineering applications, such as membrane space antennas [12,13], require the knowledge of the surface accuracy of the thin sheet during deployment, expressed as a dimensionless quadratic mean $\hat{f}$ of the out-of-plane coordinate $\hat{Y}(\hat{s})$

$$\hat{f} = \sqrt{\frac{1}{2\mathcal{F}}\int_0^{2\mathcal{F}} \hat{Y}(\hat{s})\,\mathrm{d}\hat{s}}. \tag{9}$$

From the symmetry of the deformed membrane, it follows that the quadratic mean of one half of a single creased membrane is equivalent to that of a single and multiple creased thin sheets. Therefore, in the derivation of $\hat{f}$, the expression of $\hat{Y}(\hat{s})$ from Eq. $(5)_2$ (with $i=1$) can be employed, leading to

$$\begin{aligned}\hat{f} &= \frac{2}{\lambda}\sqrt{\eta^2 - 1 + \frac{1}{\lambda}\mathcal{E}(\mathrm{am}(\lambda,\eta),\eta) - \frac{\eta^2}{\lambda}\frac{\mathrm{cn}(\lambda,\eta)\,\mathrm{sn}(\lambda,\eta)}{\mathrm{dn}(\lambda,\eta)}}\\ &\approx \sqrt{\frac{2\eta^2(\eta^2-1)(\lambda - \cosh\lambda\,\sinh\lambda)}{\lambda^3}}.\end{aligned} \tag{10}$$

2.4. Elastic energy contributions and deformation mechanisms

In the hypothesis of inextensible membranes, the two elastic mechanisms responsible for the deployment of creased sheets are (i) the fold opening, which is driven by the crease rotational stiffness k, and (ii) the panel bending, characterized by the stiffness B. Without loss of generality, we can exploit the translational symmetry of the systems with multiple creases and restrict the analysis to a membrane of length $2l$ with a single crease at $s=l$, Fig. 1c. In order to quantify the contribution of each unfolding mechanism, it is useful to compute (see Appendix A) the bending, E_b, and crease, E_c, energies as

$$\begin{aligned}E_b &= \frac{4B\lambda\eta^2}{l}\left[\lambda - \frac{\lambda}{\eta^2} + \frac{\mathcal{E}(\mathrm{am}(\lambda,\eta),\eta)}{\eta^2} - \frac{\mathrm{cn}(\lambda,\eta)\,\mathrm{sn}(\lambda,\eta)}{\mathrm{dn}(\lambda,\eta)}\right],\\ E_c &= \frac{2B^2\lambda^2\eta^2}{kl^2}\left[\mathrm{cn}\left(\lambda + \mathcal{K}(\eta),\eta\right)\right]^2.\end{aligned} \tag{11}$$

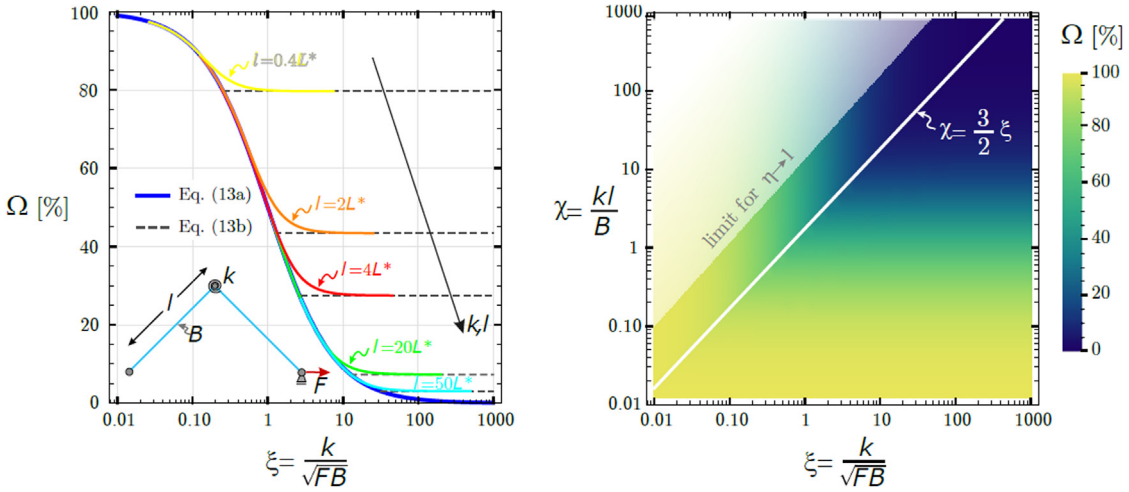

Fig. 2. Left: Contribution of crease energy Ω with respect to the total elastic energy as a function of ξ for different panel lengths $l = [0.4; 2; 4; 20; 50]L^*$, or equivalently, for different values of $\chi = l/L^* = kl/B = [0.4; 2; 4; 20; 50]$. The plot shows that at lower values of χ, the crease energy contribution prevails and the deployment response is dominated by crease opening, while at very large χ, the high percentage of bending energy suggests a preferred panel bending mechanism. At high tensioning force F, the energy contribution Ω follows Eq. (13a), while at low force the energy depends only on χ, Eq. (13b). Right: Contour plot of the simplified contribution of crease energy Ω as a function of the two dimensionless parameters ξ and χ, as expressed through Eq. (13a) (bottom-right) and Eq. (13b) (top-left), with the transition condition expressed by $\chi = 3\xi/2$.

Defining $\Gamma = E_b/E_c$ as the ratio between the two energy contributions yields

$$\Gamma = \frac{k}{\sqrt{BF}} \times \left[2\frac{\lambda(\eta^2-1)\,\mathrm{dn}(\lambda,\eta) + \varepsilon(\mathrm{am}(\lambda,\eta),\eta)\,\mathrm{dn}(\lambda,\eta) - \eta^2\,\mathrm{cn}(\lambda,\eta)\,\mathrm{sn}(\lambda,\eta)}{\eta^2\,\mathrm{dn}(\lambda,\eta)\,\mathrm{cn}^2\,(\lambda+\mathcal{K}(\eta),\eta)}\right], \tag{12}$$

so that the contribution of crease energy with respect to the total elastic energy is $\Omega = \frac{E_c}{E_c+E_b} = \frac{1}{1+\Gamma}$. From this equation, we can distinguish two limit cases that depend on the value of the applied force F

$$\Omega = \begin{cases} \dfrac{1}{1+\frac{2}{3}\frac{kl}{B}} = \dfrac{1}{1+\frac{2}{3}\chi}, & F \to 0 \quad (\eta \to \sin\dfrac{\beta}{2}) \qquad (13a) \\ \dfrac{1}{1+\frac{k}{\sqrt{FB}}} = \dfrac{1}{1+\xi}, & F \to F_{\max} \quad (\eta \to 1) \qquad (13b) \end{cases}$$

where $F_{\max}$ is the maximum force applicable to the creased sheet before it is flattened ($\eta \to 1$) and the elasticity or inextensibility assumptions cease to apply. Eqs. (13a) and (13b) suggest that there are two dimensionless parameters, namely $\chi = \frac{kl}{B}$ and $\xi = \frac{k}{\sqrt{FB}}$, which characterize the main deformation mechanism and proportion of the elastic energies. They are related through the relationship $\xi\lambda = \chi$. At low tensioning force, the parameter χ indicates that the dominant unfolding mode is crease opening when $kl < B$, or panel bending when $kl > B$, as noted from linear analyses [21,23] and as visible from Fig. 2a. However, when the applied tension increases significantly and geometric nonlinearities prevail, the contribution of crease and bending energies is defined by the parameter ξ, which combines tensioning force, crease and bending stiffnesses. In this scenario, an increase of crease rigidity k implies an increase of bending energy, while a growth of either the applied force F or the membrane bending stiffness B indicates an increase of the crease energy and the associated higher contribution of fold opening mechanism.

Eq. (13a) suggests the existence of a characteristic length scale $L^* = B/k$ [21]. When the length of each panel is small compared to L^*, the unfolding response is typical of rigid origami, mainly characterized by crease opening (Fig. 2a, yellow curve). When $l \gg L^*$, the deployment mechanism resembles a flexible origami, with higher contribution from panel bending (Fig. 2a, green and cyan curves). When $l \geq L^*$, the dominant energy contribution is panel bending at low tensioning forces, while it transitions to crease opening at high forces (Fig. 2a, orange and red curves). Fig. 2a proves that the contribution of elastic energies, defined in closed form through Eq. (12), can be well approximated by the two limit cases expressed by Eqs. (13a) and (13b), except for a limited transition region. This is due to the term within square brackets in Eq. (12), which is ≈ 1, except for very low tensioning force F. In the hypothesis that such transition domain is negligible, equating (13a) and (13b) gives the critical condition $\chi = 3\xi/2$ that defines the use of each equation in the calculation of an approximation of the crease energy contribution Ω, as shown in Fig. 2b. In particular, Eq. (13a) should be used when $\chi < 3\xi/2$, while Eq. (13b) can be employed when $\chi > 3\xi/2$. In the same figure, the faded region represents a non-admissible combination of ξ and χ, exceeding the limit of maximum applicable tension force, obtained from Eq. (4) when $\eta \to 1$. It should be noted that the non-admissible domain is almost independent of the parameter β that defines the undeformed configuration of the creased membrane.

3. Methods

3.1. Experimental

The experimental investigation consisted of three different tests: (i) uniaxial tension on dumbbell specimens to obtain material properties, (ii) uniaxial tension on rectangular strips with a single fold to characterize the crease response in terms of rotational stiffness and rest angle, and (iii) deployment tests on rectangular sheets with single and multiple creases, to validate the analytical results developed in the previous section. The experiments were performed on polyester thin films (DuPont™ Mylar® A) with thickness 100 μm and 37% opacity. The tests were carried out with an Instron 5985 electro-mechanical testing machine equipped with a 2530-50N load cell and 2713-007 self-tightening roller grips. The VIC-3D™ (Correlated Solutions, v.9) non-contact Digital Image Correlation (DIC) system was used to

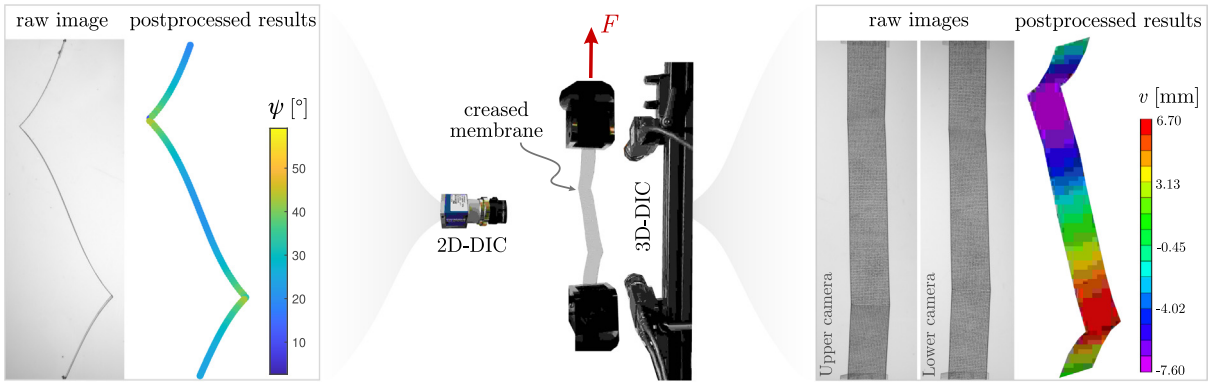

Fig. 3. Experimental setup for the quasi-static deployment of creased membranes (centre). The kinematic fields were measured through two-dimensional (left) and three-dimensional (right) digital image correlation from lateral and frontal images of the sample, respectively. Examples of post-processed results include the rotation ψ (left) and the out-of tensioning plane displacement v (right).

measure the full-field deformation of the membranes [36]. Two stereo-mounted digital cameras, Basler acA2440 75 μm 5.0 MP, equipped with Schneider Kreuznach Xenoplan 1.9/35 mm lens, and VIC-Snap (Correlated Solutions, v.9) software were employed to acquire images. Cameras set up and samples preparation were determined to enhance accuracy and minimize noise during image postprocessing. A random speckle pattern was applied to the membrane to avoid aliasing. The black speckles were created by spray paint or by depositing ink through a stamp roller, with an average speckle dimension of 8 and 5 pixels, respectively. The accuracy of the experimental results was not affected by the method used to generate the speckle pattern. Adequate contrast was achieved using white LED lights behind the specimen. The calibration images were acquired using a calibration target with 5-mm dot spacing. The experiments were performed at ambient temperature, 21.0 ± 0.4 °C.

3.1.1. Material properties

The material elastic properties were obtained by performing uniaxial tension tests on dumbbell samples (die A, ASTM D412) oriented along the machine (MD) and transverse (TD) manufacturing directions. Five tests were performed along each principal direction. The bottom end of the specimen was held fixed, while the top end was moved at a rate of 1 mm/min until a final displacement of 0.5 mm was attained. At the beginning of each test, the sample was lightly pre-tensioned with a force of 0.05 N in order to remove any initial slackness. The engineering stress was computed from the measured force, while the longitudinal and transverse nominal strains were calculated through image post-processing by using a correlation subset of 33 × 33 pixels, a step size of 7 pixels and a filter size of 11 pixels. During the tests, the maximum measured strain was 0.25%, and the material response was linear elastic. From the stress–strain response, Young's moduli were calculated as 5.07 ± 0.07 GPa and 6.36 ± 0.03 GPa for MD and TD, respectively. Similarly, from the strain values, the Poisson's ratio was obtained as 0.26 ± 0.03 for MD and 0.35 ± 0.04 for TD. Given the slightly orthotropic response, in the following experiments, only the stiffest direction was considered, and all samples were cut along the transverse direction TD, so that their average elastic properties were $E = 6.36$ GPa and $\nu = 0.35$.

3.1.2. Crease response

The crease behaviour was characterized by testing folded rectangular strips. A single crease was introduced at half-length by manually pre-folding the membrane. Subsequently, the pre-folded sheet was compressed between two platens at 1 kN for 1 min in the Instron electro-mechanical frame, before the load was removed. The crease initial opening angle γ_0 was measured using a Nikon ShuttlePix P-400Rv digital microscope after 24 hr from the end of the compression phase, in order to assess the long-term equilibrium configuration after sufficient relaxation time was allowed, such that the material viscosity on the fold opening angle was negligible [28]. Eight different samples were tested, with total lengths varying between 60 and 100 mm, widths of 10, 15, and 20 mm. The different geometries were considered to investigate their effect on the crease response.

The V-shaped folded samples were then installed in the Instron machine to perform uniaxial tension tests and characterize the fold rotational stiffness. The sample was attached to the grip through a thin transparent tape, so that the membrane was simply supported at its edges, with unconstrained rotation. A displacement of 1 mm/min was imposed at the top end of the specimen, until the membrane was fully tensioned. The tensioning force F was measured through the load cell, while the bending moment at the crease was calculated as $M_c = F\,Y_c$, where Y_c is the normal distance between the tension direction and the fold. The variation of the distance Y_c and the membrane deformed configuration were measured during the tests through two optical methods: (i) stereo DIC, aiming at calculating the three-dimensional kinematic quantities from a frontal view of the membrane, and (ii) a second approach utilizing a camera on the side to assess the two-dimensional lateral profile of the sample, Fig. 3. Matlab scripts were developed to calculate the crease opening angle γ from the DIC results, and to compute deformed shapes, end displacement δ and crease vertical position Y_c from the side view of the specimen.

3.1.3. Quasi-static deployment test

The unfolding response of creased sheets was assessed through uniaxial tension tests on membranes with single and multiple creases. The thin films were folded and installed in the testing apparatus by means of the procedures described in the previous section. Rectangular polyester strips of width $w = 15$ mm were folded such that the length l of each panel was 50 mm for the specimen with a single fold, 40 mm for doubly creased membranes, and 30 mm for thin films with three folds. The width was chosen to be negligible with respect to the length of the membranes, with $t \ll w \ll l$, as in ribbons. However, considering the translational symmetry of the sheets, boundary and loading conditions, the analysis presented is valid for different membrane widths and thicknesses, as long as the system remains slender, with $t \ll l$. The quasi-static deployment was performed at

1 mm/min displacement rate. During the experiment, the imposed displacement and tensioning force were measured by the Instron machine, while the membrane deformed configurations were obtained through the optical methods previously discussed. Four tests were performed for samples with one and two creases, two of which were measured through frontal three-dimensional DIC, and two via lateral two-dimensional digital image correlation. Since the two imaging methods yielded the same results, the deformation of the samples with three creases was acquired solely from lateral images and the custom-built Matlab code.

3.2. Finite element modelling

The finite element approach complemented the experimental study in the validation of the analytical results for the deployment of creased membranes. Similarly to the analytical solution, the translational symmetry along the width allowed to model the film as a two-dimensional geometry in Abaqus FEA 2018 (Dassault Systèmes). The creased membrane was discretized with linear beam elements with Young's modulus $E = 6.36$ GPa and Poisson's ratio $\nu = 0.35$, measured from uniaxial tension tests. The beam cross-section reproduced that of the deployment experiments, with width 15 mm and thickness 100 μm. The initial configuration of the membrane was defined by the panel length and the crease initial angle γ_0. Pinned boundary conditions were imposed at one end of the model, while a force was applied at the other edge of the beam, in the positive X direction. The crease was modelled through a connector element ('joint+rotation') with linear elastic behaviour defined by the rotational stiffness k. The results from the numerical simulations were imported in Mathematica (Wolfram, v.11) and compared with those from the analytical and experimental investigations.
The scripts developed for the analytical solution, Section 2, two-dimensional DIC, Section 3.1.2, and finite element modelling, Section 3.2, can be found at github.com/fbosi/CreasedMembranes.

4. Results and discussion

The section is devoted to the presentation of the experimental results and their comparison with the predictions obtained from the analytical models developed in Section 2 and Appendix A, and the numerical simulations described in Section 3.2.

4.1. Fold rotational stiffness

The investigation of the creased samples, after fold creation through compression test and the optical analysis of the long-term equilibrium shape, highlights that the crease opening angle for a 100 μm thick membrane is $\gamma_0 = 103.21 \pm 6.35°$. The subsequent tension tests performed on the folded thin films, as described in Section 3.1.2, show the relationship between the normalized crease bending moment M_c/w and the change in fold angle $\gamma - \gamma_0$, Fig. B.8. It can be noted that the crease response can be well described by a linear function that interpolates the discrete experimental measurements, thus validating the assumption of linear rotational spring. Therefore, the fold normalized rotational stiffness K (i.e. fold rotational stiffness k divided by the sample width w), identified by the slope of the linear fit, is obtained as $K = 3.95 \pm 0.13$ mN/deg. From Fig. B.8, the onset of a nonlinear moment–angle response can be observed in the limit of very high tensioning forces, when the membrane is almost entirely flat and the normal position of the crease is $\hat{Y}_c = Y_c/l \lessapprox 0.02$. In this limit case, the proposed solution loses accuracy as the assumption of constant rotational stiffness ceases to exist, together with the hypothesis of membrane inextensibility, since non-negligible axial strains develop.

Recent works have shown that the development of plasticity during fold creation [27] and material viscoelasticity [22] mainly affect the constant value of crease rotational stiffness and its initial opening angle γ_0, while the membrane panels remain elastic. Therefore, once the initial configuration and properties of the folds were obtained, the crease modelling neglected any nonlinear effects. However, since the initial fold angle γ_0 and the crease stiffness k are affected by the material nonlinearities and are found to be the most difficult parameters to determine experimentally, sensitivity analyses are analytically performed in order to assess the influence of the initial geometry and fold stiffness on the deployment of creased membranes. Hence, the sensitivity studies are carried out by varying the initial opening angle γ_0 and the dimensionless crease stiffness $\chi = kl/B$. These analyses are conducted on a sheet with a single fold, but are equally valid for an arbitrary number of folds thanks to the translational symmetry. As explained in detail in Appendix B, the influence of γ_0 and χ on the surface accuracy $\hat{f}$ is not significant in the ranges investigated, thus suggesting that high variability in the experimental characterization of the fold properties has a lower influence on the prediction of the deformed configuration, especially for the creased membranes that are mainly governed by the panel bending mechanism. These parametric analyses validate the assumption of negligible nonlinearities in the crease response, while providing a tool to assess their influence on the deployment response, especially at high tensioning forces. The modelling of a nonlinear crease stiffness for the regimes where the linear approximation is less effective represents an interesting extension of this study.

4.2. Deployment of membranes with single and multiple creases

The analytical predictions for the deployment of membranes with one, two and three folds are compared with the measurements obtained from tension tests to assess the accuracy of the theoretical model. It is worth noticing that the analytical and finite element predictions were perfectly overlapping, thus validating the accuracy of the developed mathematical formulation for the nonlinear response of tensioned folded sheets, Section 2 and Appendix A.

For the sheet with a single crease, Fig. 4 overlays the predicted behaviour (black and green curves) and measured response from four experiments (pink-shaded areas and red curves). The applied force F is shown as a function of the vertical crease position Y_c (a), horizontal displacement δ at the tensioning end (b), and surface accuracy f (c). All three plots exhibit a low standard deviation, which testifies a good experimental repeatability, and a very good agreement between theory and experiments. The prediction of the vertical position of the crease is in excellent agreement throughout the entire range of applied forces, while the horizontal displacement appears slightly shifted, most likely due to an initial offset and load cell inaccuracy at very low forces, but it converges towards the theoretical value at high tension. The measured surface accuracy f is in very good agreement with the theoretical value, except at very high force, where the membrane is almost fully flat and the effect of imperfections, small misalignments and resolution of the imaging technique play a significant role. Additionally, Fig. 4d superimposes the picture of the side view of the membrane during one deployment test with its analytical prediction (dashed curves), for six tensioning forces. The predicted deformed configuration captures the experimental results very well, with the two curves almost indistinguishable, except at very low forces for the reasons mentioned above.

Similar conclusions can be drawn from the comparison between the theoretical solution and the measurements for the membrane with two and three creases. Figs. 5 and 6 show the

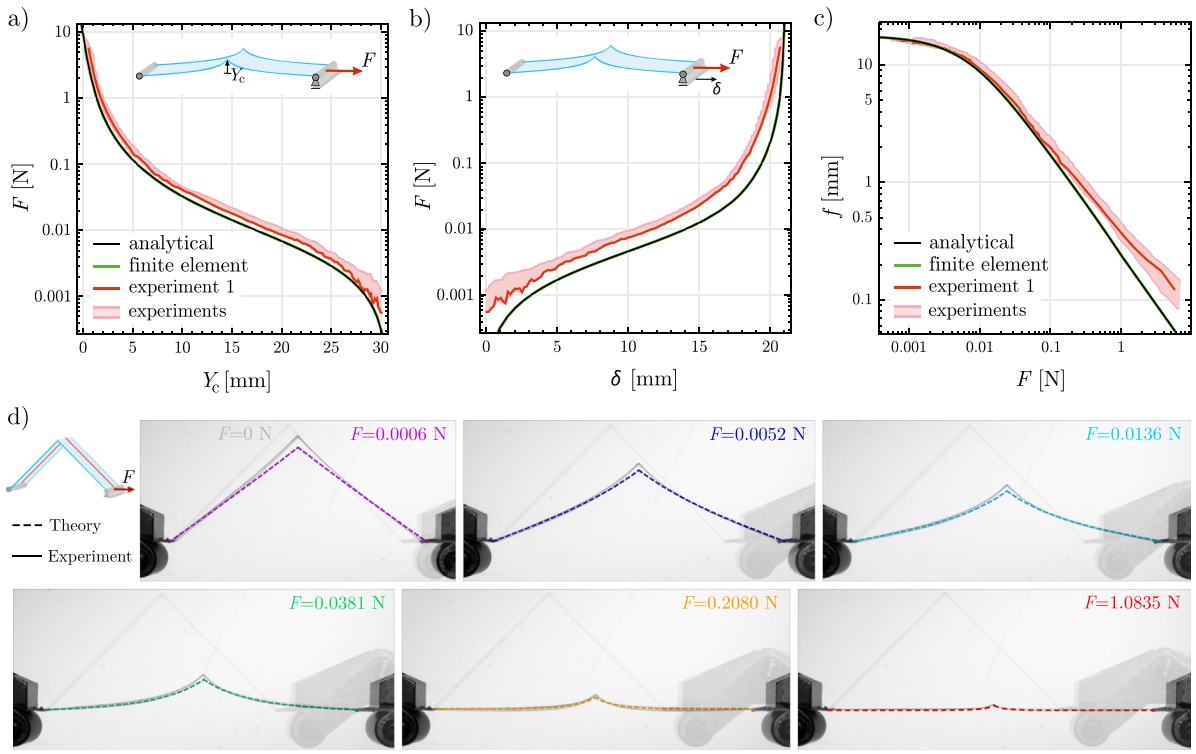

Fig. 4. Comparison between experimental results (red curve), analytical (black curve) and finite element (green curve) predictions for the deployment of a membrane with one crease: (a) tensioning force F vs. vertical position of the crease Y_c, (b) tensioning force F vs. horizontal displacement δ, and (c) surface accuracy f vs. tensioning force F. The coloured area represents the standard deviation of the four experiments performed. (d) Side views of a creased sheet during deployment, at different tensioning forces: each image shows the comparison between the experimental deformed configuration (solid) and its analytical prediction (dashed), overlaid with the undeformed configuration ($F = 0$). (For interpretation of the references to colour in this figure legend, the reader is referred to the web version of this article.)

crease absolute vertical position Y_c (a), the horizontal displacement of the tensioned end δ (b), and the quadratic mean surface accuracy f (c) as a function of the applied force F. In all plots, the experimental results (pink-shaded areas and red curves) are in excellent agreement with the analytical and finite element predictions (black and green curves, respectively), with the largest discrepancy that can be observed for the end displacement δ at the lowest forces, similarly to the sheet with a single crease. Slightly higher differences can be noticed for the membrane with three creases, especially in the $F - \delta$ plot. This can be attributed to the initial configuration, which is not perfectly symmetric due to the inherently small differences in the opening angle of each crease (see also the first images of Fig. 6d), and to the lower accuracy of the custom-made DIC script at high forces. Furthermore, Figs. 5d and 6d report the analytically calculated deformed configurations (dashed curves) juxtaposed with the lateral pictures taken during the experiments, for the sheets with two and three creases, respectively. For both systems, an excellent agreement is found over the entire membrane for the six applied forces presented. As noted before, the comparison improves at higher forces, when the influence of any initial experimental misalignment or antisymmetry diminish, and the theoretical and experimental configurations are hardly distinguishable.

Overall, the experiments performed on creased sheets with single and multiple folds testify the accuracy of the developed nonlinear model over a wide range of tensioning forces and over the entire spatial domain of the membrane. It should be noted that typical origami structures possess multiple creases converging into vertices, while the accordion-like membranes studied do not have vertices. However, this study builds the theoretical foundation for an exhaustive analysis where the interaction between sheet elasticity and the rigidity of the creases and the vertices are simultaneously considered. The characterization and modelling of the complex creases-vertices systems, outside the scope of this paper, will enable the precise modelling of three-dimensional creased systems, such as the Miura fold. The higher rigidity of the vertices is expected to affect the mechanical response and shape accuracy, especially when the combination of panel length, tensioning force, stiffness of the creases and vertices is such that the main deployment mechanism is crease opening. For origami metamaterials and structures, usually this occurs at high tensioning forces, when the membranes are almost fully deployed. If panel bending prevails, it is believed that the presented model can provide a reasonable estimate of the deployment of three-dimensional configurations with vertices, such as the Miura-ori [19], up to a certain level of loading, after which the rigidity of the vertices becomes significant.

4.3. Elastic energy contributions

For the tested membranes, we theoretically predict the elastic energy contributions and identify the proportion associated with the two mechanisms of fold opening and panel bending through Eqs. (12), (13a) and (13b). As the constituent material is the same, k and B are constants, and the two parameters that affect the deployment mechanism are the tensioning force F and the length of each panel $l = [50, 40, 30]$ mm for the membranes with one, two and three folds, respectively. Considering the sheet flexibility, and observing the deformed configurations in Figs. 4d, 5d and 6d, one would conclude that the main deployment mechanism is panel bending, which is associated with a higher contribution of

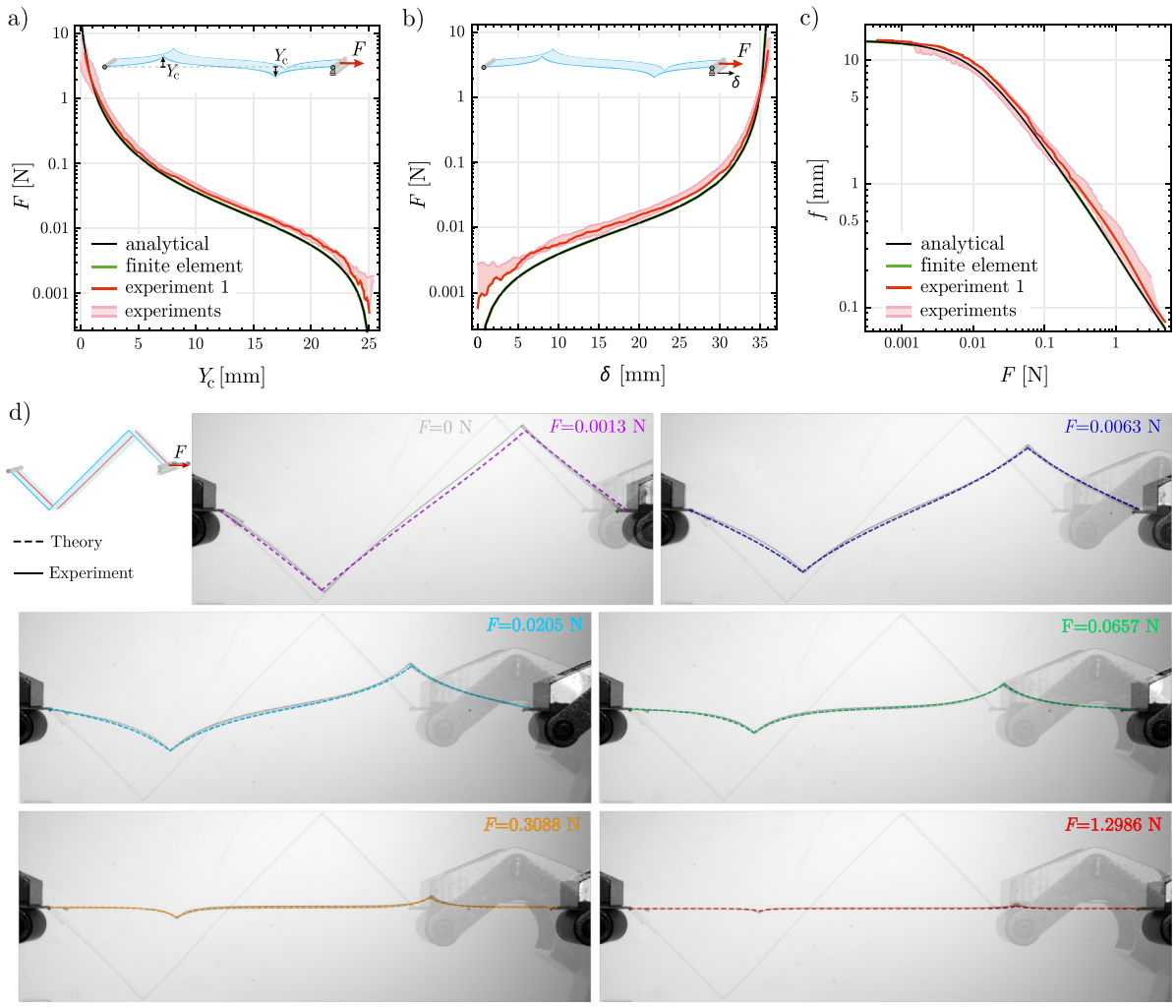

Fig. 5. Comparison between experimental results (red curve), analytical (black curve) and finite element (green curve) predictions for the deployment of a membrane with two creases: (a) tensioning force F vs. vertical position of the crease Y_c, (b) tensioning force F vs. horizontal displacement δ, and (c) surface accuracy f vs. tensioning force F. The coloured area represents the standard deviation of the two experiments performed. (d) Side views of a creased sheet with two folds during deployment, at different tensioning forces. Each image shows the comparison between the experimental deformed configuration (solid) and its analytical prediction (dashed), overlaid with the undeformed configuration ($F = 0$). (For interpretation of the references to colour in this figure legend, the reader is referred to the web version of this article.)

bending energy, and a lower contribution of crease elastic energy Ω. At low tension forces, this is confirmed by the computation of Ω through Eq. (12) and the graphs shown in Fig. A.7, where the vast majority of elastic energy is associated with sheet bending. However, an increase in applied tension produces an increase of crease energy. Eventually, the crease opening mechanism becomes the dominant one ($\Omega > 50\%$) for the membranes with two and three creases when the tension force is very high, the sheet is almost fully flat, and the increment in deployment is mainly caused by fold opening.

5. Conclusions

A mathematical formulation has been developed to predict the unfolding response of creased membranes comprising an arbitrary number of parallel folds. Within the framework of Euler's elastica theory, the developed nonlinear model accounts for the interplay between sheet bending and crease behaviour, which has been modelled as a linear rotational spring. The analytical solution was first obtained for a membrane with a single fold and then extended to account for alternating mountain and valley folds. The formulation enables the evaluation of the deformed configuration, surface accuracy and interplay between membrane bending and crease opening during deployment. In particular, the analysis of the contribution of bending and crease energies has proven the existence of two dimensionless parameters that govern the unfolding mechanism and characterize two deployment regimes. Furthermore, sensitivity analyses have been performed to assess the influence of the crease initial opening angle and the rotational stiffness on the mechanical response. Finite element analyses and experiments have been carried out to validate the developed analytical solution and the assumption of the crease constitutive model. The deployment tests were performed on three sets of 100 μm thick polyester sheets with one, two and three creases, where 2D and 3D digital image correlation techniques were used to evaluate the deformed configuration of the tensioned membranes. The experimental measurements of crease position, membrane end displacement, quadratic mean surface accuracy and deformed shape have been found in excellent agreement with the analytical predictions over a wide range of tensioning forces and thin film configurations. This proves the precision of the developed formulation, which represents an accurate tool to guide the design and assess the response of creased materials and structures undergoing deployment, such as

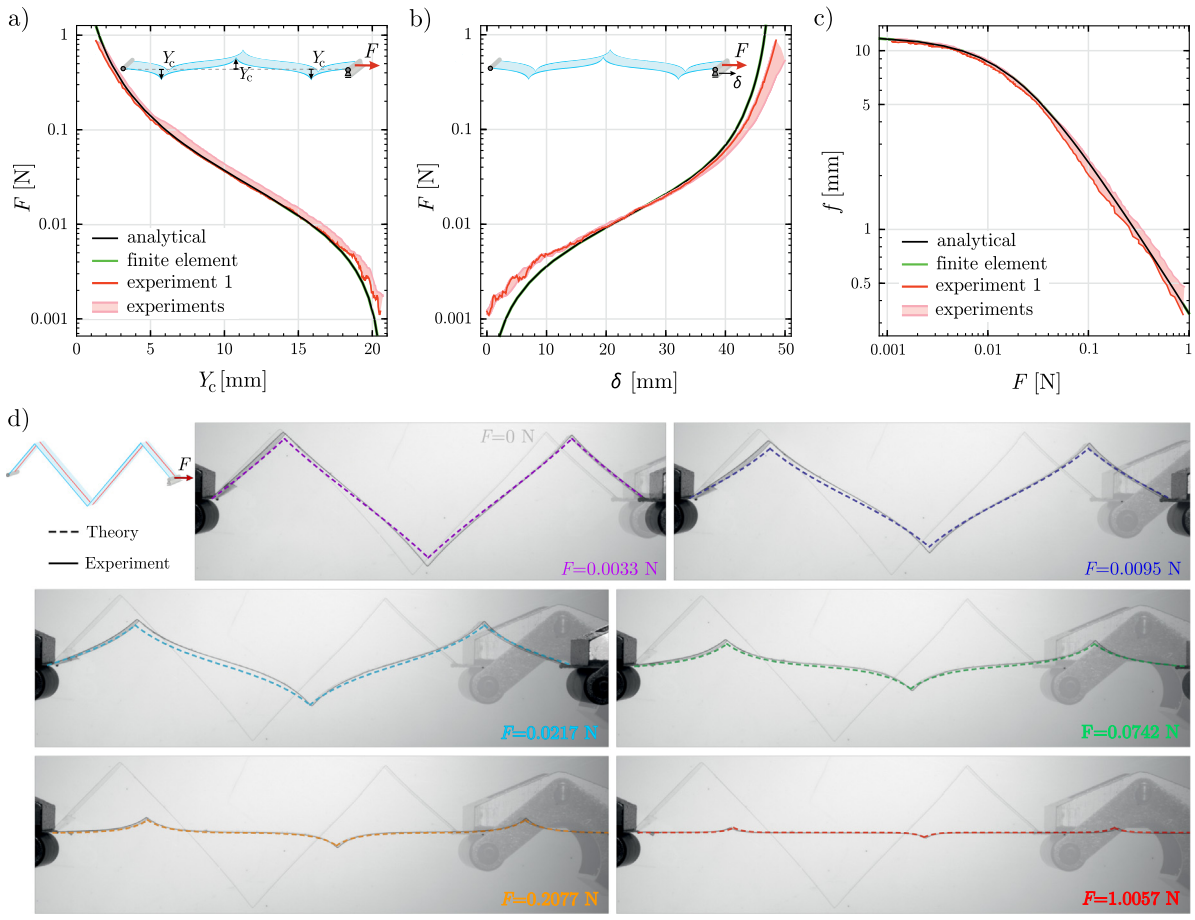

Fig. 6. Comparison between experimental results (red curve), analytical (black curve) and finite element (green curve) predictions for the deployment of a membrane with three creases: (a) tensioning force F vs. vertical position of the crease Y_c, (b) tensioning force F vs. horizontal displacement δ, and (c) surface accuracy f vs. tensioning force F. The coloured area represents the standard deviation of the four experiments performed. (d) Side views of a creased sheet with three folds during deployment, at different tensioning forces. Each image shows the comparison between the experimental deformed configuration (solid) and its analytical prediction (dashed), overlaid with the undeformed configuration ($F = 0$). (For interpretation of the references to colour in this figure legend, the reader is referred to the web version of this article.)

lightweight membranes for space structures requiring ultrahigh shape control.

Acknowledgement

F.B. acknowledges support from the Royal Society (grant no. RGS-R1-191459).

Declaration of competing interest

The authors declare that they have no known competing financial interests or personal relationships that could have appeared to influence the work reported in this paper.

Appendix A. Analytical derivation of the equilibrium equations and energy contributions for creased sheets

The equilibrium equations of the creased membrane are obtained by annealing the first variation of the total potential energy $\mathcal{V}$, Eq. (1), which can be expressed, considering integration by parts and the symmetric rotations at the crease $\theta_2(l) = -\theta_1(l)$, as

$$\begin{aligned}\delta\mathcal{V}(\theta_1,\theta_2) = &-\int_0^l \delta\theta_1\left[B\theta_1'' - F\sin(\alpha+\theta_1)\right]\mathrm{d}s\\ &+\delta\theta_1(l)\left[B\theta_1'(l)+2k\theta_1(l)\right]-B\theta_1'(0)\delta\theta_1(0)\\ &-\int_l^{2l}\delta\theta_2\left[B\theta_2'' - F\sin(\alpha-\theta_2)\right]\mathrm{d}s\\ &+\delta\theta_2(l)\left[-B\theta_2'(l)+2k\theta_2(l)\right]+B\theta_2'(2l)\delta\theta_2(2l),\end{aligned} \tag{A.1}$$

where $\delta\theta_1$ and $\delta\theta_2$ represent the variations of θ_1 and θ_2, respectively. Imposing $\delta\mathcal{V} = 0$ and introducing the supplementary angle $\beta = \pi - \alpha$, we obtain the nonlinear differential equations and boundary conditions for the first and second half of the membrane, identified by $i = 1$ and $s = [0, l]$, and $i = 2$ and $s = [l, 2l]$, respectively

$$\begin{aligned}&B\theta_i'' + (-1)^i F\sin\left[(-1)^i\theta_i+\beta\right] = 0,\\ &(-1)^i B\theta_i'(l) = 2k\theta_i(l),\\ &\theta_1'(0) = 0 \quad \text{or} \quad \theta_2'(2l) = 0.\end{aligned} \tag{A.2}$$

By introducing the auxiliary angle $\varphi_i = (-1)^i\theta_i + \beta$, the dimensionless curvilinear coordinate $\hat{s} = s/l$, load $\lambda^2 = Fl^2/B$ and

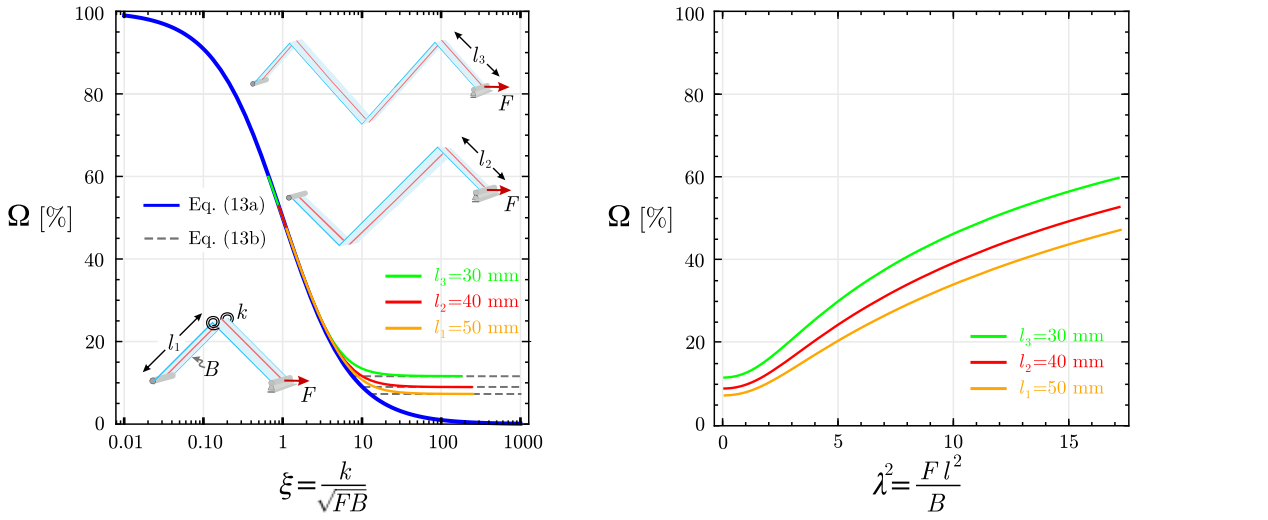

Fig. A.7. Contribution of crease energy Ω with respect to the total elastic energy as a function of ξ (left) and λ^2 (right) for the tested creased membranes, with $l = [50, 40, 30]$ mm for the sheets with one, two and three folds, respectively. B and k are material properties common to all three sets of membranes.

rotational stiffness $\chi = kl/B$, the governing system becomes

$$\begin{aligned} &\varphi_i'' + \lambda^2 \sin\varphi_i = 0 \\ &\varphi_1'(0) = 0 \quad \text{or} \quad \varphi_2'(2) = 0 \\ &\beta - \varphi_i(1) + \frac{\varphi_i'(1)\,l}{2\chi} = 0. \end{aligned} \tag{A.3}$$

The equilibrium configuration can be obtained through an analytical manipulation of Eq. (A.3) based on integration and the following change of variables

$$\begin{aligned} &\eta_1 = \sin\frac{\varphi_1(0)}{2} \quad \text{or} \quad \eta_2 = \sin\frac{\varphi_2(2)}{2} \\ &\eta_i \sin\phi_i = \sin\frac{\varphi_i}{2}, \end{aligned} \tag{A.4}$$

leading to the solution for the two halves of the membrane

$$\begin{aligned} &\varphi_1(\hat{s}) = 2\arcsin\left[\eta_1 \,\mathrm{sn}\left(\lambda\hat{s} + \mathcal{K}(\eta_1), \eta_1\right)\right], \\ &\varphi_2(\hat{s}) = 2\arcsin\left[\eta_2 \,\mathrm{sn}\left(\lambda(\hat{s}-1) + \mathcal{K}(m, \eta_2), \eta_2\right)\right], \end{aligned} \tag{A.5}$$

where sn represents the Jacobi sine amplitude function, $\mathcal{K}(\eta_i)$ and $\mathcal{K}(m, \eta_i)$ are the complete and incomplete elliptic integrals of the first kind, and m is a parameter defined as

$$m = \arcsin\left[\frac{1}{\eta_2}\sin\left(\frac{\varphi_2(0)}{2}\right)\right]. \tag{A.6}$$

Starting from Eq. (A.5), the membrane's local rotational field is described by Eq. (3), while its curvature is

$$\begin{aligned} &\theta_1'(\hat{s}) = -2\,\frac{\lambda\,\eta_1}{l}\,\mathrm{cn}\left(\lambda\hat{s} + \mathcal{K}(\eta_1), \eta_1\right), \\ &\theta_2'(\hat{s}) = 2\,\frac{\lambda\,\eta_2}{l}\,\mathrm{cn}\left(\lambda(\hat{s}-1) + \mathcal{K}(m, \eta_2), \eta_2\right), \end{aligned} \tag{A.7}$$

where cn represents the Jacobi cosine amplitude function. Substituting Eqs. (3) and (A.7) into the boundary condition at the crease, Eq. $(A.2)_2$, yields to

$$\begin{aligned} &-2\arcsin\left[\eta_1 \,\mathrm{sn}\left(\lambda + \mathcal{K}(\eta_1), \eta_1\right)\right] \\ &\quad + \beta - \frac{\lambda\,\eta_1\,\mathrm{cn}\left(\lambda + \mathcal{K}(\eta_1), \eta_1\right)}{\chi} = 0, \\ &2\arcsin\left[\eta_2 \,\mathrm{sn}\left(\mathcal{K}(m, \eta_2), \eta_2\right)\right] \\ &\quad - \beta - \frac{\lambda\,\eta_2\,\mathrm{cn}\left(\mathcal{K}(m, \eta_2), \eta_2\right)}{\chi} = 0, \end{aligned} \tag{A.8}$$

which constitute the auxiliary equations necessary to obtain the sought solution [34]. It should be noted that the integration of the system (A.3) through the change of variable (A.4), for the right side of the membrane ($i = 2$) from $\hat{s} = 1$ to $\hat{s} = 2$, provides the relationship between λ, η_2 and m

$$\lambda = \mathcal{K}(\eta_2) - \mathcal{K}(m, \eta_2). \tag{A.9}$$

Eq. (A.9) can be employed in conjunction with the properties of the Jacobi functions [35] to prove that Eqs. $(A.8)_1$ and $(A.8)_2$ are equivalent, so that $\eta_1 = \eta_2 = \eta$, as expected from the symmetry about the crease. Therefore, the unique relationship between the load parameter λ and the kinematic parameter η can be obtained by solving numerically Eq. $(A.8)_1$, which is equivalent to Eq. (4).

In the global reference frame, the membrane's deformed configuration is described by Eq. (5), whereas in the local reference frames, the dimensionless coordinates $\hat{x}_i$ and $\hat{y}_i$ of the points of the deformed membrane are calculated from the integration of the inextensibility constraints as

$$\begin{aligned} &\hat{x}_i(\hat{s}) = \frac{2\eta}{\lambda}\mathcal{A}_i \sin\beta + \mathcal{B}_i\cos\beta, \\ &\hat{y}_i(\hat{s}) = (-1)^i\left(\frac{2\eta}{\lambda}\mathcal{A}_i\cos\beta - \mathcal{B}_i\sin\beta\right), \end{aligned} \tag{A.10}$$

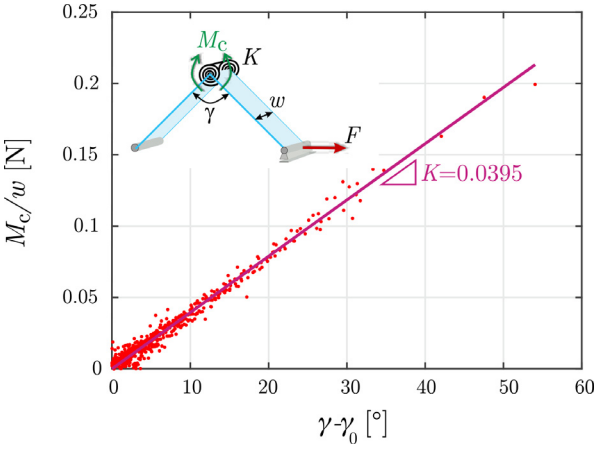

Fig. B.8. Normalized bending moment at the crease, M_c/w, reported as a function of the change in fold angle $\gamma - \gamma_0$ during uniaxial tension tests on creased samples. The cloud of points represent experimental data, fitted by a linear regression to obtain the normalized crease rotational stiffness $K = k/w$.

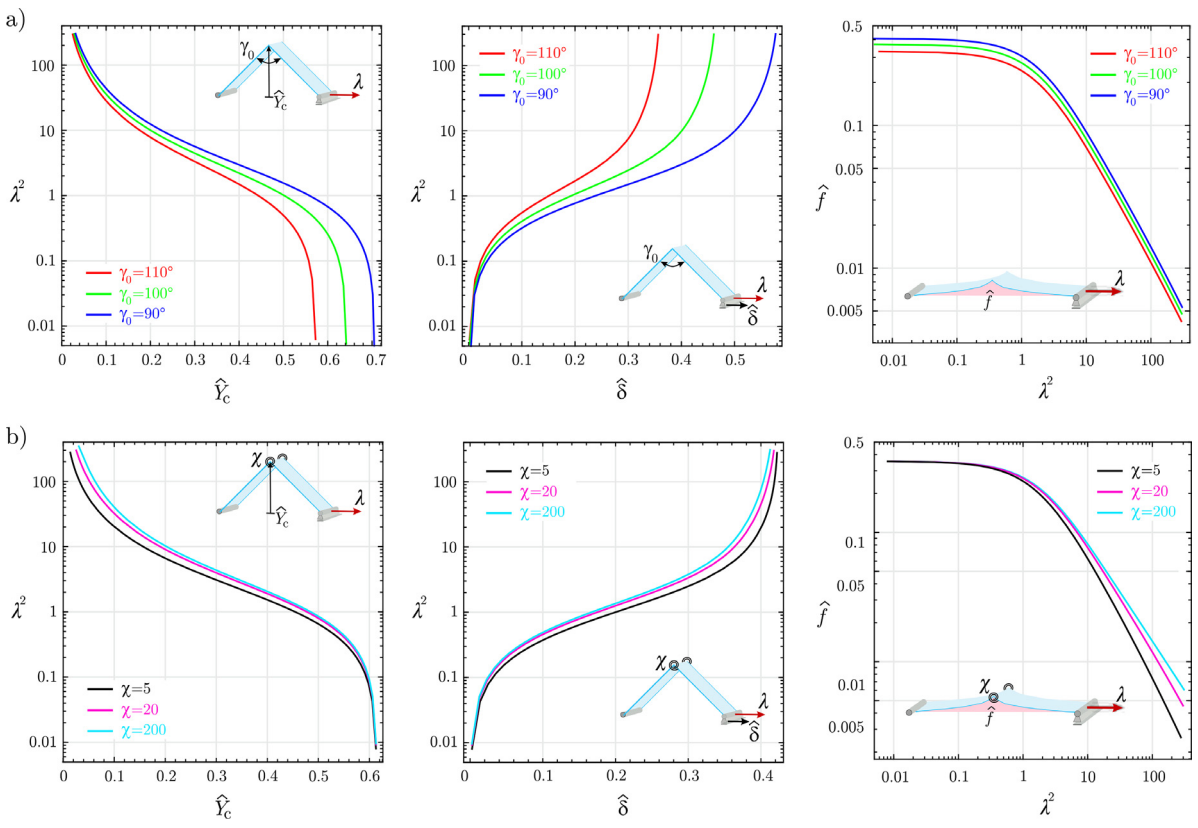

Fig. B.9. Sensitivity analysis for (a) the crease initial opening angle γ_0 and (b) the dimensionless rotational stiffness χ. Dimensionless force λ^2 vs. dimensionless vertical position of the crease $\hat{Y}_c$ (left), dimensionless force λ^2 vs. dimensionless horizontal displacement $\hat{\delta}$ (centre), and dimensionless surface accuracy $\hat{f}$ vs. dimensionless force λ^2 (right) for (a) $\gamma_0 = 110°$ (red curve), $\gamma_0 = 100°$ (green curve), $\gamma_0 = 90°$ (blue curve) and (b) $\chi = 5$ (black curve), $\chi = 20$ (pink curve), $\chi = 200$ (cyan curve). (For interpretation of the references to colour in this figure legend, the reader is referred to the web version of this article.)

where

$$\begin{aligned}
\mathcal{A}_1(\hat{s}) &= -\mathrm{cn}\left(\lambda\hat{s} + \mathcal{K}(\eta), \eta\right),\\
\mathcal{A}_2(\hat{s}) &= \mathrm{cn}(\mathcal{K}(m,\eta),\eta) - \mathrm{cn}\left(\lambda(\hat{s}-1) + \mathcal{K}(m,\eta), \eta\right),\\
\mathcal{B}_1(\hat{s}) &= -\hat{s} + \frac{2}{\lambda}\left[\mathcal{E}\left(\mathrm{am}(\lambda\hat{s} + \mathcal{K}(\eta),\eta),\eta\right) - \mathcal{E}(\eta)\right],\\
\mathcal{B}_2(\hat{s}) &= -\hat{s} + 1 + \frac{2}{\lambda}\left[\mathcal{E}\left(\mathrm{am}(\lambda(\hat{s}-1) + \mathcal{K}(m,\eta),\eta),\eta\right)\right.\\
&\quad \left. - \mathcal{E}\left(\mathrm{am}(\mathcal{K}(m,\eta),\eta),\eta\right)\right],
\end{aligned} \tag{A.11}$$

$\mathcal{E}(\eta)$ and $\mathcal{E}(m,\eta)$ are the complete and incomplete elliptic integrals of the second kind, and am represents the Jacobi amplitude function.

The bending, E_b, and crease, E_c, energies can be defined through the dimensionless coordinate $\hat{s} = s/l$ as

$$E_\mathrm{b} = 2\,l\int_0^1 \frac{M(\hat{s})^2}{2B}\mathrm{d}\hat{s}, \qquad E_\mathrm{c} = \frac{M(1)^2}{2k}, \tag{A.12}$$

where $M(\hat{s})$ and $M(1)$ are the bending moments along the membrane and at the crease, respectively. Considering Eq. (A.7), their modulus can be expressed as

$$\begin{aligned}
M(\hat{s}) &= 2\,B\frac{\lambda\,\eta}{l}\,\mathrm{cn}\left(\lambda\hat{s} + \mathcal{K}(\eta),\eta\right),\\
M(1) &= B\theta'(1) = 2\,B\frac{\lambda\,\eta}{l}\,\mathrm{cn}\left(\lambda + \mathcal{K}(\eta),\eta\right)\\
&= F\,Y_\mathrm{c} = F\frac{2\,\eta\,l}{\lambda}\mathrm{cn}\left(\lambda + \mathcal{K}(\eta),\eta\right).
\end{aligned} \tag{A.13}$$

Therefore, the bending and crease energies are expressed as in Eq. (11), while their ratio $\Gamma = E_\mathrm{b}/E_\mathrm{c}$ is defined from Eq. (12), from which the contribution of crease energy with respect to the total elastic energy becomes $\Omega = \dfrac{E_\mathrm{c}}{E_\mathrm{c}+E_\mathrm{b}} = \dfrac{1}{1+\Gamma}$.

For the three sets of membrane tested in Section 4.2, the contribution of crease elastic energy Ω is analytically computed to assess the dominant deformation mechanism, which varies depending on the tensioning force F and the length of each panel $l = [50, 40, 30]$ mm for the sheets with one, two and three folds, respectively. The plots in Fig. A.7 show Ω as a function of $\xi = k/\sqrt{FB}$ (left) and the dimensionless force $\lambda^2 = Fl^2/B$ (right). As noted in Section 2.4, an increase in panel length l leads to a greater contribution of panel bending during deployment and a decrease of Ω. Fig. A.7 (left) further demonstrates the accuracy of the simplified expressions (13a) and (13b) in capturing the energy contributions. Even though at lower tension forces the vast majority of elastic energy is associated with sheet bending, at high tension the crease opening mechanism becomes the dominant one ($\Omega > 50\%$) for the membranes with two and three creases.

Appendix B. Crease rotational stiffness and sensitivity analysis

The fold rotational stiffness per unit width, $K = k/w$, is calculated from the linear fit of the crease normalized moment–angle relationship, M_c/w vs. γ, as shown in Fig. B.8. It should be noted that the high density and scattering of experimental data at low angles is caused by the very low tensioning force, and hence bending moment in the crease, resulting from an imposed displacement at the beginning of the test. Once the tension state throughout the membrane increased, the scatter in experimental measurements decrease. Additionally, when the membrane is almost fully tensioned and the normal position of the crease is

$\hat{Y}_c = Y_c/l \lessapprox 0.02$, the rotational response of the fold becomes nonlinear, and the assumption of linear rotational spring, as well as membrane inextensibility, ceases to exist. It should be noted that the inextensibility hypothesis is consistent with the engineering application of creased membranes for space antennas, where the strain introduced in the system during deployment should be negligible to avoid plasticity, failure or delamination of the composite membranes, which can hinder both the structural and functional performances.

Sensitivity analyses are analytically and numerically performed on a sheet with a single fold to assess the influence of the fold stiffness and initial geometry on the deployment of creased membranes. In the former analysis, γ_0 is varied by $\pm 10°$ around the mean value obtained experimentally, $\gamma_0 \approx 100°$. The dimensionless crease stiffness is kept constant at $\chi = 20$, a value that approximates the rotational stiffness obtained from the experiments, Section 4.1. Fig. B.9a shows how the crease initial angle affects the dimensionless plots of force λ^2 vs. vertical position of the crease $\hat{Y}_c$ (left), force λ^2 vs. horizontal displacement of the loaded end $\hat{\delta}$ (centre), and quadratic mean surface accuracy $\hat{f}$ vs. force λ^2 (right). As expected, since the length of the membrane is kept constant, different initial angles γ_0 imply higher variability of $\hat{Y}_c$ and $\hat{\delta}$ at low and high tensioning forces, respectively. The surface accuracy $\hat{f}$, which indicates the membrane ability to reach the fully tensioned and flat configuration, shows a pronounced nonlinear decrement for high forces, and for the same value of applied force results higher for smaller γ_0.

In the second analysis, two orders-of-magnitude variation in the crease stiffness is considered, with $\chi = [5, 20, 200]$, whilst the initial opening angle is kept constant, $\gamma_0 = 100°$. Fig. B.9b reports the analogous plots as in the previous analysis, with the curves qualitatively following the same course. The figure conveys that an increase in the crease rotation stiffness produces higher $\hat{Y}_c$ and $\hat{f}$, and smaller $\hat{\delta}$, for the same tensioning force λ^2. Despite the large variation in χ, the three curves appear sufficiently close, which suggests that a high variability in the experimental characterization of χ (or k) has a lower influence on the accuracy of the prediction of the membrane deformed configuration, especially when the deployment is driven by panel bending mechanism. The main differences occur when estimating the quadratic mean surface accuracy $\hat{f}$, where the curves associated with different fold rotational rigidities diverge at higher force. In particular, stiffer creases require a very high deployment force to be opened, resulting in reduced ability to flatten the membrane.

References

[1] P.N. Bryan, J. Orban, Proteins that switch folds, Curr. Opin. Struct. Biol. 20 (4) (2010) 482–488.
[2] R. Wootton, R. Herbert, P. Young, K. Evans, Approaches to the structural modelling of insect wings, Philos. Trans. R. Soc. Lond. Ser. B Biol. Sci. 358 (1437) (2003) 1577–1587.
[3] E. Couturier, S. Courrech du Pont, S. Douady, A global regulation inducing the shape of growing folded leaves, PLoS One 4 (11) (2009) e7968.
[4] N. Magnenat-Thalmann, P. Kalra, J.L. Leveque, R. Bazin, D. Batisse, B. Querleux, A computational skin model: fold and wrinkle formation, IEEE Trans. Inf. Technol. Biomed. 6 (4) (2002) 317–323.
[5] J.L. Silverberg, A.A. Evans, L. McLeod, R.C. Hayward, T. Hull, C.D. Santangelo, I. Cohen, Using origami design principles to fold reprogrammable mechanical metamaterials, Science 345 (6197) (2014) 647–650.
[6] S. Waitukaitis, R. Menaut, B.G.-g. Chen, M. Van Hecke, Origami multistability: From single vertices to metasheets, Phys. Rev. Lett. 114 (5) (2015) 055503.
[7] S.R. Woodruff, E.T. Filipov, Bending and twisting with a pinch: Shape morphing of creased sheets, Extrem. Mech. Lett. (ISSN: 2352-4316) 52 (2022) 101656.
[8] R.J. Lang, Origami Design Secrets: Mathematical Methods for an Ancient Art, CRC Press, 2012.
[9] Y. Li, S. Pellegrino, A theory for the design of multi-stable morphing structures, J. Mech. Phys. Solids 136 (2020) 103772.
[10] D. Melancon, B. Gorissen, C.J. García-Mora, C. Hoberman, K. Bertoldi, Multistable inflatable origami structures at the metre scale, Nature 592 (7855) (2021) 545–550.
[11] F. Bosi, S. Pellegrino, Nonlinear thermomechanical response and constitutive modeling of viscoelastic polyethylene membranes, Mech. Mater. 117 (2018) 9–21.
[12] C.H. Jenkins, Gossamer Spacecraft: Membrane and Inflatable Structures Technology for Space Applications, American Institute of Aeronautics and Astronautics, 2001.
[13] W. Wang, C. Li, H. Rodrigue, F. Yuan, M.-W. Han, M. Cho, S.-H. Ahn, Kirigami/origami-based soft deployable reflector for optical beam steering, Adv. Funct. Mater. 27 (7) (2017) 1604214.
[14] M. Schenk, S.D. Guest, Geometry of miura-folded metamaterials, Proc. Natl. Acad. Sci. 110 (9) (2013) 3276–3281.
[15] M. Walker, K. Seffen, The flexural mechanics of creased thin strips, Int. J. Solids Struct. 167 (2019) 192–201.
[16] T. Jules, F. Lechenault, M. Adda-Bedia, Curving origami with mechanical frustration, Extrem. Mech. Lett. (ISSN: 2352-4316) 46 (2021) 101315.
[17] Z.Y. Wei, Z.V. Guo, L. Dudte, H.Y. Liang, L. Mahadevan, Geometric mechanics of periodic pleated origami, Phys. Rev. Lett. 110 (21) (2013) 215501.
[18] F. Haas, R.J. Wootton, Two basic mechanisms in insect wing folding, Proc. R. Soc. B 263 (1377) (1996) 1651–1658.
[19] A. Papa, S. Pellegrino, Systematically creased thin-film membrane structures, J. Spacecr. Rockets 45 (1) (2008) 10–18.
[20] K. Woo, K. Nandukar, C.H. Jenkins, Effective modulus of creased thin membranes, J. Spacecr. Rockets 45 (1) (2008) 19–26.
[21] F. Lechenault, B. Thiria, M. Adda-Bedia, Mechanical response of a creased sheet, Phys. Rev. Lett. 112 (2014) 244301.
[22] B.Y. Dharmadasa, M.W. McCallum, S. Mierunalan, S.P. Dassanayake, C.H. Mallikarachchi, F. López Jiménez, Formation of plastic creases in thin polyimide films, J. Appl. Mech. 87 (5) (2020).
[23] Z. Xia, C. Wang, H. Tan, Quasi-static unfolding mechanics of a creased membrane based on a finite deformation crease–beam model, Int. J. Solids Struct. 207 (2020) 104–112.
[24] K. Liu, G. Paulino, Nonlinear mechanics of non-rigid origami: an efficient computational approach, Proc. R. Soc. A Math. Phys. Eng. Sci. 473 (2206) (2017) 20170348.
[25] E. Barbieri, Curvature tuning in folded strips through hyperstatic applied rotations, Front. Mater. 6 (2019) 41.
[26] T. Jules, F. Lechenault, M. Adda-Bedia, Local mechanical description of an elastic fold, Soft Matter 15 (7) (2019) 1619–1626.
[27] T. Jules, F. Lechenault, M. Adda-Bedia, Plasticity and aging of folded elastic sheets, Phys. Rev. E 102 (3) (2020) 033005.
[28] B.Y. Dharmadasa, H. Mallikarachchi, F. Lopez Jimenez, Characterizing the mechanics of fold-lines in thin kapton membranes, in: 2018 AIAA Spacecraft Structures Conference, 2018, p. 0450.
[29] D. Bigoni, F. Bosi, D. Misseroni, F. Dal Corso, G. Noselli, New phenomena in nonlinear elastic structures: from tensile buckling to configurational forces, in: D. Bigoni (Ed.), Extremely Deformable Structures, Springer, Vienna, 2015, pp. 55–135.
[30] A. Love, A Treatise on the Mathematical Theory of Elasticity, Vol. 158, fourth ed., Cambridge university Press, 1927.
[31] F. Bosi, D. Misseroni, F. Dal Corso, S. Neukirch, D. Bigoni, Asymptotic self-restabilization of a continuous elastic structure, Phys. Rev. E 94 (6) (2016) 063005.
[32] F. Bosi, D. Misseroni, F. Dal Corso, D. Bigoni, Development of configurational forces during the injection of an elastic rod, Extrem. Mech. Lett. (ISSN: 2352-4316) 4 (2015) 83–88.
[33] F. Bosi, F. Dal Corso, D. Misseroni, D. Bigoni, An elastica arm scale, Proc. Roy. Soc. A 470 (2169) (2014).
[34] M. Batista, Large deflections and stability of spring-hinged cantilever beam, J. Mech. Mater. Struct. 14 (2) (2019) 295–308.
[35] P. Byrd, M. Friedman, Handbook of Elliptic Integrals for Engineers and Scientists, Springer-Verlag, 1954.
[36] M. Sutton, J. Orteu, H. Schreier, Image Correlation for Shape, Motion and Deformation Measurements: Basic Concepts, Theory and Applications, Springer, 2009.